Refractive index study of $Al_xGa_{1-x}N$ films grown on sapphire substrates

N. A. Sanford[a)]
Optoelectronics Division, ms 815, National Institute of Standards and Technology, 325 Broadway, Boulder, Colorado 80305

L. H. Robins, A. V. Davydov, and A. Shapiro
Materials Science and Engineering Laboratory, National Institute of Standards and Technology, 100 Bureau Drive, ms 8555, Gaithersburg, Maryland 20899

D. V. Tsvetkov and A. V. Dmitriev
TDI, Incorporated, Gaithersburg, Maryland 20904

S. Keller, U. K. Mishra, and S. P. DenBaars
Department of Electrical and Computer Engineering, University of California, Santa Barbara, Santa Barbara, California 93106

(Received 10 September 2002; accepted 13 June 2003)

A prism coupling method was used to measure the ordinary (n_o) and extraordinary (n_e) refractive indices of $Al_xGa_{1-x}N$ films, grown by hydride vapor phase epitaxy (HVPE) and metalorganic chemical vapor deposition (MOCVD) on sapphire, at several discrete wavelengths from 442 nm to 1064 nm. In addition, spectroscopic transmittance and reflectance, correlated with the prism coupling results, were used to measure n_o as a continuous function of wavelength between the band gap of each sample (255 nm to 364 nm, depending on Al fraction) and 2500 nm. The Al mole fractions (x), determined by energy dispersive x-ray spectroscopy (EDS), were $x=0.144$, 0.234, 0.279, 0.363, 0.593, and 0.657 for the HVPE-grown samples, and $x=0.000$, 0.419, 0.507, 0.618, 0.660, and 0.666 for the MOCVD-grown samples. The maximum standard uncertainty in the EDS-determined value of x was ± 0.02. The maximum standard uncertainty in the refractive indices measured by prism coupling was ± 0.005 and a one-Sellmeier-term equation was adequate to fit the wavelength dependence of n_e from 442 nm to 1064 nm. Due to the spectral proximity of the absorption edge, the wavelength dependence of n_o measured by spectroscopic transmittance/reflectance (correlated with the prism-coupling results), from the band gap of each sample to 2500 nm, was fit with a two-Sellmeier-term equation. © *2003 American Institute of Physics.*
[DOI: 10.1063/1.1598276]

I. INTRODUCTION

Hexagonal $Al_xGa_{1-x}N$ alloys are important for the development of laser diodes and light-emitting diodes operating at green to ultraviolet wavelengths. The material is uniaxial and optically anisotropic. Reliable data on the refractive index and birefringence as functions of wavelength and Al mole fraction (parameter x), including reasonable estimates of the measurement uncertainties, will enable more accurate modeling of the optical and optoelectronic properties of devices. Spectroscopic transmittance and reflectance (STR) have been used to measure the ordinary refractive index of $Al_xGa_{1-x}N$ films.[1–3] Spectroscopic ellipsometry (SE) has been used to measure the refractive index and extinction coefficients of $Al_xGa_{1-x}N$ films[4–6] and to measure both ordinary and extraordinary refractive indices of GaN films.[7] The STR and SE methods, when performed with white-light illumination, have the advantage that the optical properties can be measured as a quasicontinuous function of wavelength throughout a large wavelength range. The drawback of STR and SE is that an independent film thickness measurement is often required for accurate refractive index determination. Accurate thickness measurements are difficult and usually require cross sectioning or other destructive sample preparation. As an example of the measurement uncertainty of SE results, in Ref. 7, the quoted uncertainty of the film thickness is 1241.6 nm $\pm$ 42 nm and the refractive index uncertainty is approximately $\pm 2\%$. Recent work that combined the methods of SE, spectroscopic reflectance, and transmission electron microscopy (TEM) reduced the number of adjustable parameters required to quantify the refractive index and birefringence of GaN films grown by molecular-beam epitaxy (MBE) on GaAs and 6H–SiC.[8]

The prism-coupled waveguide mode (PCWM) analysis described in the present study provides a straightforward technique for evaluation of the refractive index, birefringence, and film thickness that does not require a separate film thickness measurement to attain high accuracy. The PCWM method enables an unambiguous measurement of the film refractive index and thickness at a given wavelength if the optical waveguide formed by the film/substrate combination supports at least two guided transverse electric (TE) modes (polarized parallel to the film surface) or at least two transverse magnetic (TM) modes (polarized normal to the film surface) and the film is homogeneous.[9] PCWM methods

a)Electronic mail: sanford@boulder.nist.gov

TABLE I. Listing of sample number, growth method (M=MOCVD and H=HVPE), and Al mole fraction x as determined by EDS.

Sample No.	1	2	3	4	5	6	7	8	9	10	11	12
Growth	M	H	H	H	H	M	M	H	M	H	M	M
x	0.00	0.144	0.234	0.279	0.363	0.419	0.507	0.593	0.618	0.657	0.660	0.666

have recently been applied to $Al_xGa_{1-x}N$ films grown on *c*-plane sapphire substrates by metalorganic chemical vapor deposition (MOCVD) and MBE.[10–13] However, as detailed in the results that follow in this article, the solutions for extraordinary (n_e) refractive indices in birefringent optical waveguides are dependent upon the solutions for the ordinary (n_o) indices, a fact often ignored by many authors. Therefore, the analysis must be performed carefully in order to minimize the computed error in n_e. Additional problems have been encountered with the calibration of Al mole fraction in the evaluation of the composition dependence of refractive index in $Al_xGa_{1-x}N$ films. A convenient method is to employ optical absorption and assume a particular form for the bowing of the fundamental band gap as a function of Al mole fraction where the latter has been separately established by x-ray diffraction, analytical electron microscopy, or optical spectroscopy.[14–16] However, as pointed out by Özgür, bowing parameters may depend upon the fabrication method used to grow the $Al_xGa_{1-x}N$ films.[13] It is therefore important to explore alternative direct methods to calibrate the Al mole fraction and correlate these results with refractive index measurements.

In this article, we present our developed methods of birefringent optical waveguide analysis and apply them to determine the refractive index and birefringence of $Al_xGa_{1-x}N$ films, grown on sapphire substrates by hydride vapor phase epitaxy (HVPE) and MOCVD, at a discrete set of (laser) wavelengths from 442 nm to 1064 nm. A discussion of the uncertainties involved in these measurements and computations is also given, and we have adopted the nomenclature used in the description of uncertainties as summarized in National Institute of Standards and Technology (NIST) guidelines.[17] In addition, we show that normal-incidence STR measurements, when analyzed by a curve-fitting method and correlated with the optical waveguide results, can be used to determine the ordinary refractive index over a wider wavelength range than the discrete-wavelength PCWM analysis alone. We estimate that the largest standard uncertainty in the refractive index measurements of the $Al_xGa_{1-x}N$ films is ± 0.005. The Al mole fraction x for the samples was measured using energy dispersive x-ray spectroscopy (EDS), and the largest standard uncertainty in the absolute value is x is ± 0.02.

II. SAMPLE PREPARATION AND ENERGY DISPERSIVE X-RAY SPECTROSCOPY ASSESSMENT OF THE Al MOLE FRACTION

Samples were grown using MOCVD and HVPE methods. All substrates used were c-plane sapphire. For the MOCVD grown samples, the AlGaN layers were deposited at 100 Torr using the precursors trimethyl gallium (TMGa), trimethyl aluminum (TMAl), and ammonia (NH_3). The TMAl and NH_3 flows were kept constant at 40×10^{-6} mol/min and 67×10^{-3} mol/min, respectively. The TMGa flow was varied between 28×10^{-6} mol/min and 56×10^{-6} mol/min. After high-temperature treatment of the sapphire substrate in hydrogen, an 18 nm AlGaN nucleation layer was grown at 600 °C followed by the deposition of the main AlGaN layer at 1100 °C.

The HVPE samples were prepared using a modified growth technique.[18,19] The growth system was equipped with an atmospheric-pressure quartz, horizontal hot-wall reactor, and a resistively heated furnace. Ar was used as the diluting gas, and ammonia was used as the nitrogen source. Hydrogen chloride gas was flowed through Al and Ga source channels with subsequent mixing and reacting with NH_3 in the growth zone to form the $Al_xGa_{1-x}N$ layer.

The Al composition of the samples was examined using a scanning electron microscope (SEM) equipped with EDS capability. Experimentation with the electron accelerating voltage revealed that the use of 4 keV excitation would ensure that the EDS signal originated from the $Al_{1-x}Ga_xN$ films without contamination from the sapphire substrates. At 4 keV, however, the EDS analysis may become sensitive to the contribution from the sample surface containing native gallium/aluminum oxynitrides. This could potentially contribute to a systematic error in determining the composition. Further studies of a low-voltage excitation on the accuracy of the EDS analysis are underway. The EDS spectra were normalized using data from GaN and AlN reference samples. Corrections accounting for atomic number, absorption, and secondary fluorescence (ZAF corrections) were performed by the NORAN (Middleton, WI) MICROZ microanalysis software. At least three measurements were made from different locations (near center and corners) on a sample and the results were averaged. The samples were roughly 5 mm square. Each spectrum was recorded with a counting time of 100 s. The typical maximum variation in x across a sample was ± 0.003. However, the estimated largest standard uncertainty in the EDS-determined value of x was ± 0.02 for the $Al_xGa_{1-x}N$ samples. Table I gives a summary of growth method and x value for the samples examined in the present study.

III. PRISM-COUPLED WAVEGUIDE MODE METHOD: FUNDAMENTAL THEORY

We assign the Cartesian $x-y$ axes to the plane of the film and the z axis normal to the surface of the film. The z axis conforms to the optical c axes of the film and substrate. Maxwell's equations describing optical fields in the structure are

$$\nabla \times \mathbf{H} = \varepsilon_o \tilde{\varepsilon} \cdot \frac{\partial \mathbf{E}}{\partial t}, \tag{1a}$$

$$\nabla \times \mathbf{E} = -\mu_o \frac{\partial \mathbf{H}}{\partial t}, \tag{1b}$$

$$\nabla \cdot \mathbf{D} = 0. \tag{1c}$$

The dielectric tensor is expressed as a dyad and is given by

$$\tilde{\varepsilon} = \hat{x}\hat{x}(n_o)^2 + \hat{y}\hat{y}(n_o)^2 + \hat{z}\hat{z}(n_e)^2. \tag{2}$$

Boldface quantities are vectors as the context indicates, and $\hat{x}$, $\hat{y}$, and $\hat{z}$ are unit vectors along their respective axes. **E** is the electric field, **H** is the magnetic field strength, μ_o is the magnetic permeability, and ε_o is the permittivity of free space. The electric displacement **D** is given by $\mathbf{D} = \varepsilon_o \tilde{\varepsilon} \cdot \mathbf{E}$. The ordinary and extraordinary refractive indices n_o and n_e are replaced by n_o^s and n_e^s in the sapphire substrate and by n_o^g, and n_e^g in the $Al_xGa_{1-x}N$ films. The refractive index in the air superstrate is set equal to unity. Cartesian subscripted italic forms of **E**, **H**, and **D** represent components of these vectors along the axis indicated by the subscript. Ordinary polarized modes have their electric field vectors in the $x-y$ plane while extraordinary polarized modes are substantially polarized along the z axis. The convention from integrated optical technology labels these polarization states as TE and TM, respectively. For convenience, we will constrain guided modes to propagate along the x axis. Manipulation with the component form of Eqs. (1a)–(1c) permits the derivation of wave equations describing TE and TM mode propagation. With the vacuum optical wavelength given by λ, and $k = 2\pi/\lambda$, the propagation of the TE modes is described by

$$\partial_{xx}^2 E_y + \partial_{zz}^2 E_y + k n_o^2 E_y = 0 \tag{3a}$$

and the propagation of TM modes is described by

$$\partial_{xx}^2 H_y + \left(\frac{n_e^2}{n_o^2}\right) \partial_{zz}^2 H_y + k n_e^2 H_y = 0. \tag{3b}$$

The solutions for both cases involve plane waves. For the TE modes, the solutions in the air, the $Al_xGa_{1-x}N$ films, and the sapphire substrate are

$$E_y = \begin{cases} A_a e^{i(k_x x - \omega t)} e^{-\kappa_a (z-L)} & \text{in the air,} \quad (4a) \\ A_g e^{i(k_x x - \omega t)} \cos[k_z (z+\delta)] & \text{in the } Al_xGa_{1-x}N \text{ film, and} \quad (4b) \\ A_s e^{i(k_x x - \omega t)} e^{\kappa_s z} & \text{in the sapphire substrate.} \quad (4c) \end{cases}$$

In Eqs. (4a)–(4c), $k_x = Nk$, where N is defined as the effective index of a TE mode and is bounded by $n_o^s < N < n_o^g$. The transverse wave vector components κ_a, κ_s, and k_z are all functions of N through dispersion relations derived by direct substitution of Eqs. (4a)–(4c) into Eq. (3a). With $H_x = (i/\mu_o \omega)\partial_z E_y$, the continuity of E_y and H_x at the boundaries $z = 0$, L leads to a transcendental equation linking N, L (film thickness), n_o^s, and n_o^g. This equation permits self-consistent computation of n_o^g and L provided that at least two modes with distinct values of N can be excited in the $Al_xGa_{1-x}N$ film. It is not necessary to compute values for the amplitudes A_g, A_s, A_a, or the phase factor δ. The transcendental equation enabling a solution for the effective indices for the TE modes is

$$\tan\left[kL\sqrt{(n_o^g)^2 - N^2}\right] = \sqrt{(n_o^g)^2 - N^2}\left[\frac{\sqrt{N^2-1} + \sqrt{N^2 - (n_o^s)^2}}{(n_o^g)^2 - N^2 - \sqrt{N^2-1}\sqrt{N^2-(n_o^s)^2}}\right]. \tag{5a}$$

Using similar procedures, noting that $E_x = (-i/\varepsilon_o \omega n_o^2)\partial_z H_y$, and defining the effective index for a TM mode as η, the corresponding transcendental equation for TM modes is

$$\tan\left[kL\left(\frac{n_o^g}{n_e^g}\right)\sqrt{(n_e^g)^2 - \eta^2}\right] = \frac{\sqrt{(n_e^g)^2 - \eta^2}}{n_o^g n_e^g}\left[\frac{\sqrt{\eta^2-1} + \dfrac{\sqrt{\eta^2 - (n_e^s)^2}}{n_o^s n_e^s}}{\dfrac{(n_e^g)^2 - \eta^2}{(n_o^g n_e^g)^2} - \dfrac{\sqrt{\eta^2-1}\sqrt{\eta^2-(n_e^s)^2}}{n_o^s n_e^s}}\right]. \tag{5b}$$

Note that the distinguishing feature of Eq. (5b) is that the birefringence of the $Al_xGa_{1-x}N$ film and sapphire substrate are explicitly present. Therefore, in order to calculate the extraordinary index n_e^g of an $Al_xGa_{1-x}N$ film, one must first compute n_o^g and L, include n_o^g as an input parameter for the TM solution, and then verify that the TM solution returns an equivalent value for L. Some authors use an approach whereby the TM solutions are obtained by assuming isotropic media with film and substrate refractive indices set equal to n_e^g and n_e^s, respectively.[10–13] The error introduced by using such an approach will be discussed later.

IV. PRISM-COUPLED WAVEGUIDE MODE METHOD: EXPERIMENTAL PROCEDURE AND DATA ANALYSIS

The effective indices of the guided modes were measured as follows. Consider Fig. 1(a) describing a prism cou-

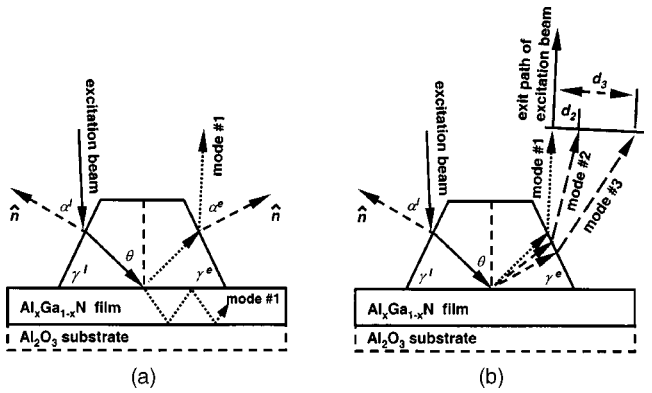

FIG. 1. (a) The use of a prism coupler to launch a single guided mode (labeled as mode No. 1) into a $Al_xGa_{1-x}N$ film grown on a sapphire substrate. The launch angle of the mode with respect to the prism normal $\hat{\mathbf{n}}$ is α^ℓ, the prism apex angle on the launch side is γ^ℓ, and the launch angle of mode No. 1 within the prism with respect to the film/substrate normal is θ. On the output side of the prism, the corresponding apex angle γ^e and mode emission angle α^e are shown. If the prism is perfectly symmetric, $\gamma^\ell = \gamma^e$ and $\alpha^\ell = \alpha^e$. The propagating mode is illustrated by a zigzag line in the film. A prism coupler such as this will simultaneously couple light into and out of guided modes. The dashed arrow emerging from the exit face illustrates light emerging from the prism at an angle α^e. This corresponds to the exit ray of the excitation beam overlaying a portion of the out-coupled guided mode. (b) An illustration showing that in a waveguide that supports three modes, launching into one mode characterized by launch angle α_1^ℓ, corresponding to emitted mode No. 1, will result in coupling into the other available modes that appear on the viewing screen at locations d_2 and d_3 as shown.

pler used to launch a single TE mode of effective index N propagating in the $Al_xGa_{1-x}N$ film. Snell's law requires for TE modes that $N = n_e^p \sin\theta$, where n_e^p is the extraordinary index of the prism and θ is the angle of incidence at the prism–film interface. The mode launch angle external to the prism (of apex angle γ_ℓ) is denoted by α^ℓ and $\sin\alpha^\ell = n_e^p \sin(\theta - \gamma_\ell)$. It then follows that $N = \sin\alpha^\ell \cos\gamma_\ell + \sin\gamma_\ell \sqrt{(n_e^p)^2 - \sin^2\gamma_\ell}$. The same equation may be used to calculate η for a single TM mode by equating α^ℓ with the launch angle of the mode and replacing n_e^p with the ordinary index of the prism, n_o^p.

For all of the PCWM results presented in this article, a symmetric rutile prism was used. The value of the prism apex angle on the launch side was $\gamma_\ell = 49.92° \pm 0.03°$. The value of the apex angle γ_e of the exit side of the prism was $\gamma_e = 50.04° \pm 0.03°$. The rutile refractive indices were calculated using the Sellmeier equations of Rams *et al.*[20] An alternative method for measuring the effective indices is to measure the angles α_i^e at which the out-coupled modes emerge with respect to the prism normal. The symmetric prism illustrated in Fig. 1(a) facilitates simultaneous incoupling and outcoupling of the modes, and the conventions for the angles α^ℓ and α^e for a particular mode are indicated in Fig. 1. Using this arrangement, we typically observed that many modes were simultaneously excited and coupled out of a $Al_xGa_{1-x}N$ film even though the launch condition was optimized for a single particular mode. This effect is evidence for considerable optical scattering in the films and, in some instances, scattering between the TE and TM polarized modes also occurred. The modes were observed as bright bands falling on a screen placed perpendicular to the excitation beam leaving the prism and appear similar to those illustrated in Ref. 10. We typically positioned the screen 200 mm from the output facet of the prism. The angles α_i^e of the out-coupled modes were calculated by measuring the displacements d_i of their corresponding bands from the excitation beam spot on the screen, computing the angles $\beta_i = \arctan(d_i/200)$, and then calculating $\alpha_i^e = \alpha^e + \beta_i$ where α^e is the angle between the excitation beam leaving the prism and the normal to the prism exit face. This construction is illustrated in Fig. 1(b). In the actual evaluation of β_i, account is taken of the small displacements of the modes along the prism face as illustrated schematically in Fig. 1(b). Note that the convention for the signs of these angles is consistent with the usage of Ref. 9. Due to diffraction and scattering, the width of the bands appearing on the observation screen was typically 0.5 mm for the lower-order modes at a wavelength $\lambda = 632.8$ nm at the 200 mm viewing distance. This width persists even with precautions taken for weak prism coupling to prevent prism-induced perturbations to the measurements.[9] The higher-order modes, particularly those close to cutoff, often displayed wider bands, up to 3 mm in some of the worst instances, at the 200 mm viewing distance. Therefore, the measured uncertainties in α_i^e that are introduced by the width of the bands may vary with wavelength and the order of the mode. The higher-order modes displaying greater scattering than the lower-order modes at all wavelengths is further evidence of the effect of scattering from irregularities in the film/substrate interface. This follows since the magnitude of the optical electric field of the higher-order modes is greater in this region than that of the lower-order modes.

A least-squares fitting procedure was used to solve Eq. 5(a) for n_o^g and L with the measured effective indices of TE modes used as input. A graphical example of a solution is illustrated in Fig. 2(a) for the case of sample No. 6 (MOCVD growth, $x = 0.419$) supporting six TE modes at a wavelength $\lambda = 632.8$ nm. The vertical solid lines appearing in the graph indicate the measured effective indices of the guided modes. The simultaneous intersection of these lines with the solutions of Eq. (5a) is obtained with $n_o^g = 2.243$ and $L = 1.312$ μm. Using this value of n_o^g as input for the solution of the TM case, the least-squares fitting procedure was then used to calculate $n_e^g = 2.279$. The corresponding value for L computed for the TM case was $L = 1.313$ μm. A graph illustrating the TM solution is illustrated in Fig. 2(b). A discussion of the uncertainty in these measurements is now given.

V. PRISM-COUPLED WAVEGUIDE MODE METHOD: SOURCES OF ERROR

The primary source of uncertainty in these calculations is the measurement of the effective indices N and η. The major factors that contribute to these uncertainties are the uncertainties in the mode positions d_i, the prism apex angles γ_ℓ and γ_e, and the prism refractive index. In most instances, the uncertainty in locating the mode positions at the 200 mm view distance is ± 0.5 mm to ± 0.75 mm depending upon the mode being measured. This uncertainty is increased by

roughly ± 0.5 mm due to the spatial separation of the modes at the exit face of the prism. The largest standard uncertainty in the prism apex angle was $\pm 0.03°$. The uncertainties in d_i, γ_ℓ, and γ_e are statistical (type A uncertainties in the parlance of Ref. 17). Rams *et al.*[20] determined the refractive index of rutile by measuring the critical angle for total reflection at the rutile/$LiNbO_3$ interface. They give the (room-temperature) uncertainty in the refractive index as ± 0.001 and base this number on the uncertainty in the refractive index for $LiNbO_3$. Considering all of these uncertainties, we have calculated the largest standard uncertainties in N and η as a function of effective index and wavelength. The conclusion of this analysis is that, at the short wavelength extreme (442 nm–500 nm), the largest standard uncertainties in N and η vary from approximately ± 0.004 to ± 0.005 between the low-order and high-order modes, respectively. At the long-wavelength extreme (750 nm–1064 nm), the largest standard uncertainties in N and η vary from approximately 0.003 for low-order modes to approximately 0.005 for the high-order modes. We then used these results in calculating the resulting uncertainties in the transcendental solutions for n_o^g, n_e^g, and L. We calculated that variations of n_o^g and n_e^g of ± 0.005 and variations of L of ± 15 nm would typically accommodate the span of the largest standard uncertainties in N and η in the numerical and graphical solutions for refractive index and film thickness. Based on these observations, we assign the largest standard uncertainty of ± 0.005 to n_o^g and n_e^g, and the largest standard uncertainty of ± 15 nm to L. By comparison, the prism coupling studies described in Refs. 11–13 all give estimated uncertainties of ± 0.01 for the refractive indices and give no uncertainty estimate for sample thickness. Given the refractive index differential between the AlGaN films and the sapphire substrate, the uncertainty in the sapphire refractive index is a less important issue in the calculations. The refractive index of the sapphire substrates was calculated using the Sellmeier equations of Malitson and Dodge.[21] We found that variations of the sapphire index by as much as ± 0.02 had only a negligible effect on the computed results of n_o^g, n_e^g, and L for the sample with the highest Al mole fraction (66.6%), provided that the effective index of the highest-order mode was greater than the substrate index by at least 0.15. For samples with lower Al content, the uncertainty in computed values of index and thickness, resulting from uncertainty in the substrate index, is even less.

It is instructive to consider the consequences of assuming an isotropic approximation for the TM solution case whereby the birefringence-induced dependence of the TM solutions on the TE solutions is ignored and the film and substrate refractive indices are set equal to their respective extraordinary indices. Returning to the TM example illustrated in Fig. 2(b) (where the full birefringence was taken into account), but computing the result using the isotropic approximation, we find that essentially the same value of n_e^g is computed in either case. However, the value of L returned is roughly 25 nm less than that computed when the full birefringence is included. Performing the same comparison for cases where only a few modes are present reveals comparable discrepancies in L with discrepancies in n_e^g increasing to a few parts in 10^{-3}. Therefore, given the inherent uncertainties involved in locating the mode positions due to the optical scattering in the films and the resulting uncertainties in the computed precision for L, n_o^g, and n_e^g described earlier, adopting an isotropic approximation for the computation of n_e^g may be acceptable for the present level of $Al_xGa_{1-x}N$ film quality. Indeed, as discussed in Sec. VIII, the data presented in Tables II (a, b) illustrate the results of the computation of n_o^g, n_e^g and the values of L computed from the TE and TM cases for all of the samples measured. For simplicity, we abbreviate n_o^g by n_o and n_e^g by n_e. These results indicate that for some samples, there are inconsistencies as large as 25 nm in the computed values for L even if the full birefringence is included in the calculations. On the other hand, the data also show many examples where the use of the full media birefringence in the solution procedure for TM modes would return values of L differing by only a few nm (and in some cases, the deviation is zero) from those computed via TE mode data. These issues will be discussed further in Sec. IX.

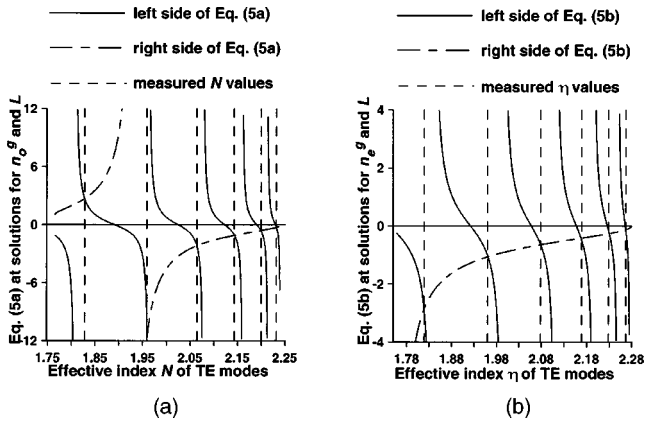

FIG. 2. (a) A graphical representation of the solution of Eq. (5a) describing the effective indices N of TE modes for sample No. 6 at 632.8 nm. The dashed vertical lines on the graph are the measured values of effective indices N for the TE modes. The simultaneous intersection of these lines with the curves representing the left-and right-hand sides of Eq. (5a) correspond to the solution for $n_o = 2.243$ and $L = 1.312$ μm as given in Table II (a). (b) A graph illustrating the solution of Eq. (5b) showing the measured effective indices of the TM modes at 632.8 nm for sample No. 6 and the associated simultaneous solution of $n_e = 2.279$ and $L = 1.313$ μm as given in Table II (b).

VI. SPECTROSCOPIC TRANSMITTANCE AND REFLECTANCE: EXPERIMENTAL PROCEDURE

Normal-incidence STR measurements were performed in a Cary-14 spectrophotometer (Varian, Cary, NC) equipped with deuterium, tungsten–halogen, and tungsten light sources and lead sulfide and photomultiplier tube detectors having a full wavelength range 190 nm to 2500 nm. 11 of the 12 samples were characterized by STR; sample No. 10 was omitted because the back substrate surface was not polished, hence, transmittance measurements were not possible. For transmittance measurements, the diameter of the aperture that defined the probe area was 3.8 mm; spectra were normalized by taking the ratio of the sample transmittance to the transmittance of an empty aperture of equal diameter. In the wavelength range below the band gap, where the sample

TABLE II(a). Ordinary refractive index n_o and sample thickness L (in micrometers) computed by PCWM for the set of 12 $Al_xGa_{1-x}N$ samples. The number of TE modes m observed at a particular wavelength and the resulting values for n_o and $L(\mu m)$ calculated at that wavelength are given. For example, reading to the right-hand side in the row beginning with 442 nm and the column headed by sample No. 1, the entries immediately following "n_o" lists the ordinary refractive index at 442 nm for the MOCVD-grown GaN sample with $x=0.000$, the entries immediately following "L" list the value of the thickness calculated for this sample using the TE mode data at 442 nm, and the entry immediately following "m" indicate the number of 442 nm TE modes used in the calculation.

		Sample No.											
λ		1	2	3	4	5	6	7	8	9	10	11	12
442	n_o	2.471	2.412	2.380	2.358	2.327	2.313	2.283	2.251	2.243	2.233	2.232	2.227
	L	2.115	0.739	0.702	0.433	0.449	1.310	1.174	0.555	0.955	0.622	1.018	1.013
	m	10	5	5	3	3	6	5	3	5	3	5	5
457.9	n_o	2.454	2.399	2.366	2.347	2.319	2.311	2.274	2.249	2.240	2.222	2.220	2.216
	L	2.168	0.743	0.699	0.448	0.460	1.304	1.173	0.546	0.952	0.631	1.031	1.020
	m	10	4	4	2	2	8	6	3	5	3	5	5
488	n_o	2.429	2.380	2.347	2.325	2.302	2.290	2.258	2.230	2.223	2.212	2.216	2.211
	L	2.115	0.748	0.701	0.445	0.455	1.307	1.181	0.557	0.961	0.625	1.014	1.017
	m	7	5	4	3	3	8	5	3	5	3	5	5
514.5	n_o	2.413	2.363	2.334	2.314	2.291	2.278	2.250	2.225	2.215	2.205	2.204	2.201
	L	2.110	0.745	0.703	0.447	0.447	1.307	1.174	0.544	0.954	0.622	1.037	1.022
	m	11	5	4	3	2	7	5	3	5	3	5	5
532	n_o	2.397	2.356	2.327	2.308	2.278	2.272	2.246	2.215	2.212	2.204		2.199
	L	2.187	0.740	0.694	0.430	0.451	1.311	1.181	0.549	0.951	0.636		1.020
	m	12	5	4	3	3	7	6	3	5	3		5
632.8	n_o	2.360	2.319	2.294	2.271	2.254	2.243	2.222	2.193	2.186	2.177	2.176	2.174
	L	2.126	0.744	0.701	0.454	0.456	1.312	1.169	0.551	0.957	0.622	1.024	1.024
	m	10	4	4	2	2	6	5	3	4	3	4	4
677	n_o									2.184			
	L									0.956			
	m									4			
690	n_o	2.345	2.305	2.281	2.266	2.243	2.236	2.213	2.185		2.170		2.165
	L	2.180	0.745	0.705	0.440	0.448	1.310	1.187	0.549		0.653		1.024
	m	7	3	3	2	2	5	5	2		3		4
750	n_o	2.337	2.295	2.272	2.252	2.233	2.229	2.206	2.178	2.172	2.160	2.163	2.162
	L	2.113	0.741	0.703	0.455	0.463	1.321	1.180	0.547	0.960	0.627	1.021	1.019
	m	6	3	3	2	2	4	3	2	4	2	4	4
850	n_o	2.325	2.282	2.258			2.219	2.195	2.170	2.167		2.156	2.156
	L	2.107	0.743	0.706			1.308	1.170	0.548	0.951		1.029	1.010
	m	6	3	3			4	4	2	3		3	3
1064	n_o	2.304	2.274	2.244			2.210	2.182	2.157	2.155		2.147	2.144
	L	2.147	0.735	0.702			1.316	1.190	0.560	0.960		1.026	1.031
	m	6	2	2			3	2	2	2		3	3

transmittance is low, the measurement range was extended by inserting metal–mesh neutral density (ND) filters in the spectrophotometer reference beam. The ND filters allowed measurements of transmittances as low as 10^{-6}. For reflectance measurements, the aperture diameter was 5.1 mm. (Note that some samples slightly underfilled the reflectance aperture.) The reflectance spectra were normalized by an "indirect V–W" method, as described in another publication.[22] The advantage of the indirect V–W method, which requires two "working standard" mirrors, is that the reflectance spectra of the standards need not be known *a priori*.

Run-to-run variations in the optical alignment, and in the voltage gain ratio between the sample and reference channels, were found to produce variations of up to 10% in the magnitude of the normalized transmittance or reflectance signal. These variations were observed when comparing the results of successive data acquisition runs for the same sample. In addition, the magnitude of the normalized reflectance was reduced for samples which were too small to completely fill the 5.1 mm reflectance aperture. On the other hand, the line shape of the normalized transmittance or reflectance spectrum (i.e., the ratio of the intensities at any two wavelengths within a given spectrum) was reproducible to high accuracy for successive runs.

VII. SPECTROSCOPIC TRANSMITTANCE AND REFLECTANCE: DATA ANALYSIS AND SOURCES OF ERROR

The STR data were analyzed by least-squares curve-fitting of a model with several adjustable parameters to the measured transmittance and reflectance spectra. In the model, the wavelength dependence of the ordinary refractive index is described by a two-Sellmeier-term function with four adjustable parameters,

$$n_o(\lambda)=\sqrt{1+A_1^*\lambda^2/[\lambda^2-(B_1^*)^2]+A_2^*\lambda^2/[\lambda^2-(B_2^*)^2]}. \tag{6}$$

Additional details of the functional analysis of the STR data are discussed in another publication.[22]

TABLE II(b). Extraordinary refractive index n_e and sample thickness L computed by PCWM for the set of 12 $Al_xGa_{1-x}N$ samples.

		Sample No.											
λ		1	2	3	4	5	6	7	8	9	10	11	12
442	n_e	2.514	2.452	2.417	2.400	2.362	2.355	2.323	2.293	2.284	2.272	2.272	2.271
	L	2.126	0.751	0.703	0.462	0.468	1.314	1.181	0.568	0.965	0.628	1.041	1.037
	m	14	4	4	2	2	8	7	3	6	2	7	7
457.9	n_e	2.493	2.438	2.405	2.385	2.358	2.343	2.316	2.282	2.279	2.265	2.266	2.264
	L	2.193	0.754	0.708	0.459	0.455	1.307	1.189	0.554	0.956	0.635	1.026	1.026
	m	10	3	4	2	2	9	8	3	5	3	6	6
488	n_e	2.465	2.414	2.384	2.372	2.333	2.327	2.299	2.267	2.266	2.255	2.252	2.248
	L	2.131	0.755	0.703	0.457	0.471	1.314	1.192	0.564	0.955	0.629	1.025	1.033
	m	10	3	4	2	2	8	6	3	5	3	5	6
514.5	n_e	2.445	2.397	2.370	2.353	2.324	2.315	2.289	2.258	2.253	2.241	2.240	2.241
	L	2.127	0.770	0.704	0.455	0.459	1.315	1.196	0.556	0.965	0.631	1.030	1.024
	m	12	3	4	2	2	8	6	3	5	3	6	5
532	n_e	2.435	2.390	2.361	2.340	2.316	2.308	2.282	2.251	2.248	2.236		2.234
	L	2.200	0.764	0.707	0.454	0.456	1.315	1.183	0.556	0.963	0.650		1.025
	m	13	3	4	3	3	7	6	3	5	4		5
632.8	n_e	2.395	2.352	2.328	2.308	2.286	2.279	2.254	2.232	2.222	2.210	2.211	2.213
	L	2.130	0.748	0.701	0.459	0.463	1.313	1.183	0.554	0.968	0.635	1.031	1.027
	m	9	3	4	2	2	6	5	2	4	3	4	4
677	n_e									2.217			
	L									0.967			
	m									4			
690	n_e	2.380	2.341	2.315	2.294	2.276	2.269	2.246	2.218		2.206		2.207
	L	2.200	0.747	0.705	0.460	0.453	1.304	1.187	0.554		0.659		1.021
	m	9	2	3	2	2	4	5	2		3		4
750	n_e	2.371	2.330	2.305	2.283	2.263	2.265	2.239	2.215	2.209	2.200	2.200	2.197
	L	2.145	0.749	0.705	0.467	0.473	1.311	1.185	0.568	0.965	0.624	1.033	1.031
	m	8	3	3	2	2	4	4	2	4	2	4	4
850	n_e	2.355	2.315	2.295			2.254	2.230	2.207	2.201		2.192	2.191
	L	2.133	0.752	0.706			1.330	1.186	0.559	0.953		1.034	1.030
	m	6	3	3			4	4	2	3		3	3
1064	n_e	2.342	2.300	2.279			2.236	2.216	2.200	2.193		2.180	2.182
	L	2.148	0.744	0.706			1.320	1.185	0.560	0.972		1.028	1.028
	m	6	2	2			2	3	2	2		3	2

Model transmittance and reflectance spectra (dotted lines) for an ''idealized'' $Al_xGa_{1-x}N$/sapphire sample (with optically flat, parallel surfaces, i.e., no ''thickness taper'' and no optical scatter from the interfaces) with the same optical constants and same average film thickness as sample No. 6 are shown in Figs. 3(a) and 3(b). Model transmittance and reflectance spectra (dotted lines) for an idealized $Al_xGa_{1-x}N$/sapphire sample with the same optical constants and same average film thickness as sample No. 8 are shown in Figs. 3(c) and 3(d). Note that T and R are plotted as functions of inverse wavelength or wave number, 1/λ, in Fig. 3; selected wavelength values are shown on the top x axis.

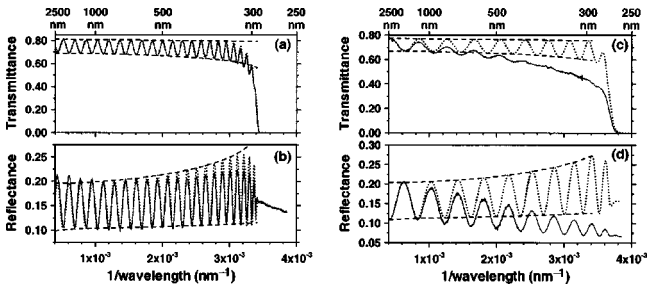

FIG. 3. Transmittance and reflectance spectra of sample Nos. 6 and 8, plotted as functions of 1/wavelength. The solid curves are the experimental results. The dotted curves show model calculations for ideal samples with the same optical properties (refractive index and absorption coefficient) as the actual samples, but no optical scatter or thickness variation. The dashed curves are the calculated transmittance and reflectance envelope functions for the ideal samples. (a) Sample No. 6, transmittance. (b) Sample No. 6, reflectance. (c) Sample No. 8, transmittance. (d) Sample No. 8, reflectance.

Several features of the model spectra shown in Fig. 3 are correlated with $n_o(\lambda)$. First, interference fringes occur in both transmittance and reflectance at wavelengths longer than the band gap (293.4 nm for sample No. 6, 272.0 nm for sample No. 8). The index-thickness product, $n_o(\lambda)L$, is obtained from the interference fringes by $n_o(\lambda)L = 1/(2\Delta_{\text{fringe}}(1/\lambda))$, where $\Delta_{\text{fringe}}(1/\lambda)$ is the interference fringe period in the wave number plot.

The upper and lower bounds of the interference patterns in the model spectra, which are sometimes referred to as ''envelope functions,'' are shown as dashed lines in Fig. 3. The envelope functions $T_{\text{upper}}(\lambda)$, $T_{\text{lower}}(\lambda)$, $R_{\text{upper}}(\lambda)$, and $R_{\text{lower}}(\lambda)$ in the model spectra (of the idealized samples) are given by

$$T_{\text{upper}}(\lambda) = (1+\delta_T)[2n_S(\lambda)/(n_S^2(\lambda)+1)], \tag{7a}$$

$$T_{\text{lower}}(\lambda) = (1+\delta_T)[4n_S(\lambda)n_o^2(\lambda)/((n_o^2(\lambda)+1)(n_o^2(\lambda) + n_S^2(\lambda)))^2], \tag{7b}$$

$$R_{\text{upper}}(\lambda)=(1+\delta_R)[1-4n_S(\lambda)n_o^2(\lambda)/((n_o^2(\lambda)+1)\times(n_o^2(\lambda)+n_S^2(\lambda)))^2], \quad (7c)$$

$$R_{\text{lower}}(\lambda)=(1+\delta_R)[1-2n_S(\lambda)/(n_S^2(\lambda)+1)]. \quad (7d)$$

Equations (7a)–7(d) were derived on the basis of phase-coherent multiple reflections in the $Al_xGa_{1-x}N$ layer and phase-randomized multiple reflections in the sapphire substrate. The envelope functions, as defined here, do not include the effect of optical absorption. Hence, the envelope functions (dashed curves in Fig. 3) deviate from the full model functions (dotted curves in Fig. 3) at wavelengths near the band gap, where optical absorption is significant.

In Eq. (7a)–7(d), the factors $(1+\delta_T)$ and $(1+\delta_R)$ represent the scaling errors due to run-to-run optical alignment variations, as discussed herein. The scaling factors are eliminated by calculating the ratio of the upper to lower envelope functions, $T_{\text{upper}}(\lambda)/T_{\text{lower}}(\lambda)$ or $R_{\text{upper}}(\lambda)/R_{\text{lower}}(\lambda)$. The envelope function ratios depend only on $n_S(\lambda)$, which is known, and $n_o(\lambda)$; therefore, $n_o(\lambda)$ can be determined. Error propagation analysis (discussed in Ref. 22) shows that the uncertainty in $n_o(\lambda)$ determined from $T_{\text{upper}}(\lambda)/T_{\text{lower}}(\lambda)$ is approximately ± 0.005 to ± 0.010 for an uncertainty of ± 0.001 to ± 0.002 in $T_{\text{upper}}(\lambda)$ and $T_{\text{lower}}(\lambda)$. The uncertainty in $n_o(\lambda)$ determined from $R_{\text{upper}}(\lambda)/R_{\text{lower}}(\lambda)$ is much larger, approximately ± 0.040 to ± 0.080, for an equivalent uncertainty of ± 0.001 to ± 0.002 in $R_{\text{upper}}(\lambda)$ and $R_{\text{lower}}(\lambda)$.

The measured transmittance and reflectance spectra, plotted as solid lines in Fig. 3, show small but observable deviations from the model spectra for sample No. 6 and larger deviations from the model spectra for sample No. 8. These deviations are ascribed primarily to two effects: First, optical scatter from the air/film, film/substrate, and substrate/air interfaces, which reduces both the transmitted and reflected intensities in the specular directions; second, thickness taper or ''thickness wedge,'' which gives rise to a spatial variation of the factor $2n_o(\lambda)L$ and, hence, reduces the amplitude of the interference fringes.

As discussed in Ref. 22, the model functions for STR were modified by adding several parameters to account for the effects of interface scatter and thickness taper. The fitted model functions are not shown in Fig. 3 because the fits cannot easily be distinguished from the data (i.e., the quality of the fits is very good). It was necessary to make some simplifying assumptions, which may not be completely accurate, to incorporate the effects of surface scatter and thickness taper in the model. Inaccurate modeling of these effects may give rise to systematic errors in the fitting parameters, including $n_o(\lambda)$ and L. The product $n_o(\lambda)L$ is, however, still determined from the interference fringe spacing, and is thus unaffected by the possible modeling inaccuracies. Hence, any systematic error in $n_o(\lambda)$ is given by a constant scaling factor, $n_o^{\text{STR}}(\lambda)=n_o^{\text{true}}(\lambda)(1+\varepsilon_{\text{STR}})$, and the systematic error in L is given by the inverse scaling factor, $L^{\text{STR}}=L^{\text{true}}/(1+\varepsilon_{\text{STR}})$.

The fractional error, ε_{STR}, can be estimated from independent measurements of either L or $n_o(\lambda)$. However, film thickness measurements usually require destructive sample preparation such as cross sectioning. Further, in a sample with significant thickness taper, it is difficult to ensure that the thickness measurements probe the same sample region (and, hence, the same thickness) as STR. Independent measurements of $n_o(\lambda)$, such as the PCWM measurements and analysis in the present study, are thus preferred for estimating and eliminating ε_{STR}. Comparison of the PCWM and STR values of $n_o(\lambda)$ at one wavelength would be sufficient to estimate ε_{STR}. However, as discussed herein, PCWM measurements were done at eight to ten distinct wavelengths for each sample. Therefore, in order to best correlate the STR and PCWM results, the STR values of $n_o(\lambda)$ for each sample were rescaled by a factor that minimizes the sum of squared differences between $n_o^{\text{STR}}(\lambda)$ and $n_o^{\text{PCWM}}(\lambda)$ at the PCWM (laser) wavelengths.

After the rescaling of the STR values, the 2σ value of $n_o^{\text{STR,cor}}(\lambda_i)-n_o^{\text{PCWM}}(\lambda_i)$ for all 104 data points was found to be 0.0063; the largest difference for any data point was -0.0096 (for sample No. 4 at $\lambda_i=690$ nm, $n_o^{\text{STR,cor}}=2.2564$, $n_o^{\text{PCWM}}=2.2660$). Further, the distribution of differences is normal in a statistical sense; the magnitude of $n_o^{\text{STR,cor}}(\lambda_i)-n_o^{\text{PCWM}}(\lambda_i)$ lies between 0 and 1σ for 71 data points (68% of all data points), and between 1σ and 2σ for 29 data points (28%). This result is consistent with a 2σ measurement uncertainty of ± 0.0044 for both $n_o^{\text{STR,cor}}(\lambda_i)$ and $n_o^{\text{PCWM}}(\lambda_i)$, in good agreement with the uncertainty estimates given herein.

TABLE III. Ordinary refractive index values at $\lambda_i=632.8$ nm, measured by PCWM and STR methods. Column 1: Sample index number (repeated from Table I). Column 2: PCWM results, $n_o^{\text{PCWM}}(\lambda_i)$. Column 3: STR results before correlation with PCWM, $n_o^{\text{STR,uncor}}(\lambda_i)$. Column 4: STR results after rescaling to minimize root-mean-squared deviation from PCWM, $n_o^{\text{STR,cor}}(\lambda_i)$. Column 5: Estimate of systematic error in the uncorrelated STR results (column 3), $\varepsilon_{\text{STR}}=(n_o^{\text{STR,uncor}}(\lambda_i)/n_o^{\text{STR,cor}}(\lambda_i))-1$. Note that the 2σ uncertainty is estimated to be ± 0.005 for both $n_o^{\text{PCWM}}(\lambda_i)$ and $n_o^{\text{STR,cor}}(\lambda_i)$.

Sample No.	n_o^{PCWM}	$n_o^{\text{STR,uncor}}$	$n_o^{\text{STR,cor}}$	ε_{STR} (%)
1	2.360	2.3071	2.3594	−2.22
2	2.319	2.2859	2.3190	−1.43
3	2.294	2.2231	2.2932	−3.06
4	2.271	2.2509	2.2694	−0.82
5	2.254	2.2000	2.2547	−2.43
6	2.243	2.2262	2.2455	−0.86
7	2.222	2.2132	2.2193	−0.28
8	2.193	2.1643	2.1935	−1.33
9	2.186	2.1887	2.1876	+0.05
11	2.176	2.1824	2.1764	+0.27
12	2.174	2.1886	2.1740	+0.67

Table III shows the ordinary refractive index values obtained by PCWM and STR, at $\lambda_6=632.8$ nm, for the 11 samples that were characterized by both methods. The PCWM results, $n_o^{\text{PCWM}}(\lambda_6)$ [repeated from Table II(a)], the independent or uncorrelated STR results, $n_o^{\text{STR,uncor}}(\lambda_6)$, the corrected STR results (after correlation with PCWM), $n_o^{\text{STR,cor}}(\lambda_6)$, and the estimated error in the uncorrelated STR results, $\varepsilon_{\text{STR}}=n_o^{\text{STR,uncor}}(\lambda_6)/n_o^{\text{STR,cor}}(\lambda_6)-1$, are shown in columns 2 to 5 respectively. The most negative value of ε_{STR} is -3.06%, for sample No. 3; the most positive value is $+0.67\%$, for sample No. 12; more samples show negative,

TABLE IV. Coefficients of the two-Sellmeier-term expression, Eq. (6), for the ordinary refractive index from STR (after scaling to minimize the deviation between the STR and PCWM refractive index values). Note that coefficients A_1^* and A_2^* are dimensionless, while B_1^*, B_2^*, and λ_{GAP} are in nanometer units.

Sample No.	A_1^*	B_1^* (nm)	A_2^*	B_2^* (nm)	λ_{GAP} (nm)
1	0.083	354.8	4.085	180.3	363.9
2	0.117	326.2	3.930	165.4	339.6
3	0.201	302.2	3.769	151.6	324.7
4	0.152	296.6	3.658	173.7	323.0
5	0.243	278.0	3.590	143.0	305.3
6	0.141	277.6	3.641	153.0	293.4
7	0.148	263.3	3.533	150.6	279.6
8	0.238	246.7	3.363	138.1	272.1
9	0.236	241.0	3.337	140.5	262.3
11	0.197	238.3	3.331	142.0	256.4
12	0.182	237.7	3.337	142.3	254.6

rather than positive, values of ε_{STR}. It thus appears that the uncorrelated STR analysis tends to underestimate n_o.

Table IV shows the coefficients of the two-Sellmeier-term fits to $n_o^{STR,cor}(\lambda)$ [Eq. (6)] for each sample characterized by both STR and PCWM. For convenience, the band-gap wavelengths are also listed in Table IV. Note that the ratio of the first resonant wavelength in the Sellmeier fit (B_1^*) to the band gap falls in the range 0.91 to 0.97, and the ratio of the second resonant wavelength (B_2^*) to the band gap falls in the range 0.47 to 0.56.

VIII. WAVELENGTH-DEPENDENT REFRACTIVE INDEX AND BIREFRINGENCE RESULTS

The PCWM analysis methods developed in Secs. III and IV were used to compute n_e, n_o, and film thickness L at a number of discrete wavelengths for the samples summarized in Table I. The lasers used in the PCWM data collection included HeCd (442 nm), Ar ion (457.9, 488, and 514.5 nm), doubled Nd:Yag (532 nm), semiconductor (677 nm), Ti:Sapphire (690, 750, and 850 nm), and Nd:Yag (1064 nm). Not all of the samples were examined at identical wavelengths due to the availability of the various laser sources and the fact that some samples (samples 4, 5, and 10) were too thin to support more than one mode at wavelengths greater than 800 nm. Prism-coupling measurements at wavelengths below 400 nm were precluded since the optical absorption of rutile becomes significant. The results for the computed ordinary refractive indices for the samples, and the corresponding values for thickness, are displayed in Table II(a). Results for the computed extraordinary index and thickness are given in Table II(b). As observed in Tables II(a) and II(b), large differences in thickness may result when comparing solutions for different wavelengths. This often occurs since some of the films were tapered in thickness and, with mounting and remounting samples and switching laser sources, it was rare that precisely the same location on a sample could be returned to for each test wavelength used. TE and TM effective index data at a particular wavelength were always collected at a common location on a sample, however. Thus, a more relevant comparison for consistency in the computed sample thickness for the TE and TM cases is to consider the results of the calculations at a given wavelength.

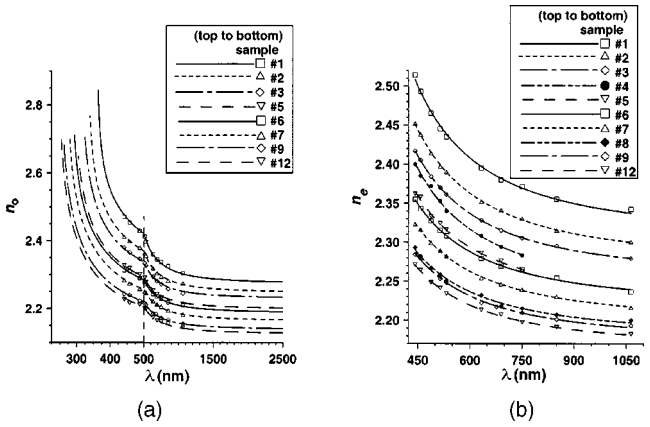

FIG. 4. (a) Wavelength dependence of the ordinary index n_o for selected $Al_xGa_{1-x}N$ samples. Solid, dashed, and dashed–dotted curves: $n_o(\lambda)$ plotted as a continuous function from the band gap of each sample to 2500 nm; functions are the two-term-Sellmeier fits to the STR data (after correlation with the PCWM results; see Tables III and IV). Symbols (squares, triangles, and diamonds): PCWM measurements of $n_o(\lambda)$ at discrete laser wavelengths. Notice the change in the wavelength scale at 500 nm (vertical dashed line); the scale is expanded at shorter wavelengths, from 250 nm to 500 nm, to better display the dispersion in this range. (b) Wavelength dependence of the extraordinary index n_e for the selected $Al_xGa_{1-x}N$ samples appearing in (a) in addition to sample Nos. 4 and 8. Curves: $n_e(\lambda)$ plotted as a continuous function from 442 nm to 1064 nm (the wavelength range for the PCWM measurements); functions are the one-term-Sellmeier fits to the PCWM data (see Table V). Symbols: PCWM measurements of $n_e(\lambda)$ at discrete laser wavelengths.

The effect of Si doping on the refractive index in MOCVD-grown $Al_xGa_{1-x}N$ films was considered. Here, two samples of nearly identical Al concentration were examined, for which one was Si doped to a concentration of roughly 5×10^{18} cm^{-3} (sample No. 11) and the other sample was not intentionally doped (sample No. 12). The Al mole fraction measured by EDS was $x=0.660$ for the Si-doped sample while, for the not intentionally doped companion sample, EDS indicated $x=0.666$. The results for these samples are also given in Tables II(a) and II(b) and illustrate that there is a resolvable offset in n_o between the two samples that is consistent with the EDS-resolved difference in x. The difference in n_e between the two samples, however, is not resolved. These results suggest that, at least for material within the vicinity of $x=0.660$, there is a negligible effect of Si doping on the ordinary refractive index of $Al_xGa_{1-x}N$ for a dopant concentration near 5×10^{18} cm^{-3}, while there is apparently some effect on the extraordinary index.

Graphs of n_e as a function of wavelength for all of the samples examined are given in Fig. 4(b). These data were fit to the one-Sellmeier-term equations

$$n_e=\sqrt{1+A_e\lambda^2/(\lambda^2-B_e^2)}, \tag{8}$$

whose coefficients are given in Table V. For the samples examined in the present study, the deviation between a similar one-Sellmeier-term equation describing n_o and the two-Sellmeier-term equation [Eq. (6)] derived from the correlated

TABLE V. Coefficients of the one-Sellmeier-term fits for n_e, Eq. (8), calculated by PWCM for the set of 12 $Al_xGa_{1-x}N$ samples used in the present study. Coefficients A_e are dimensionless, while B_e are in nanometer units.

Sample No.	A_e	B_e
1	4.321	189.2
2	4.164	181.4
3	4.080	175.3
4	3.973	180.2
5	3.922	168.9
6	3.919	163.7
7	3.827	159.7
8	3.748	151.1
9	3.720	152.6
10	3.676	151.8
11	3.679	150.9
12	3.683	148.9

STR/PCWM analysis is not significant. Therefore, we use Eq. (6) to describe the results for n_o as described in Secs. VI and VII.

IX. DISCUSSION

When comparing refractive index data reported by different researchers, it is important to keep in mind that any fitting equation should not be considered valid outside the wavelength range of the data used to establish the fit. Thus, the one-Sellmeier-term fits to the waveguide mode measurements for n_e [Eq. (8)] are valid from 442 nm to 1064 nm. For n_o, the two-term-Sellmeier fits derived from correlated STR/PCWM measurements [Eq. (6)] are valid from the band-gap wavelength of each sample at the short-wavelength end, which varies from 363 nm for GaN (sample No. 1) to 253 nm for $Al_{0.666}Ga_{0.334}N$ (sample No. 12), to 2500 nm at the long-wavelength end. Similar cautions about the validity range of semiempirical fitting equations have been raised by other authors.[16] We compared the results presented in this article for the MOCVD-grown GaN/sapphire sample (sample No. 1) to earlier work that used SE[7] and PCWM[11,13] methods to measure the refractive indices of GaN films grown on sapphire, and other earlier work that used SE to measure the refractive indices of GaN films grown by MBE on SiC.[8] The comparisons are illustrated in Fig. 5(a), where a graph of the two-term-Sellmeier equation that was used to fit the n_o results for sample No. 1 is compared with ordinary index data given in Refs. 7, 8, 11, and 13. In Fig. 5(b), a comparison of the PCWM results for n_e [described by the one-Sellmeier-term equation of Eq. (8)] for sample No. 1 is compared to the results for the extraordinary refractive of GaN given also in Refs. 7, 8, 11, and 13. For clarity, the SE results of Ref. 8 are displayed in Figs. 5(a) and 5(b) with solid points separated by 0.1 eV intervals.

For comparisons of n_o, the results of the correlated STR/PCWM of the present work and the other PCWM results are all consistent to within approximately 0.015. The agreement of the correlated STR/PCWM results for n_o with the SE results is much better. In fact, the SE results of Goldhahn *et al.*[8] agree within experimental error with the correlated STR/PCWM results while the SE results of Yu *et al.*[7]

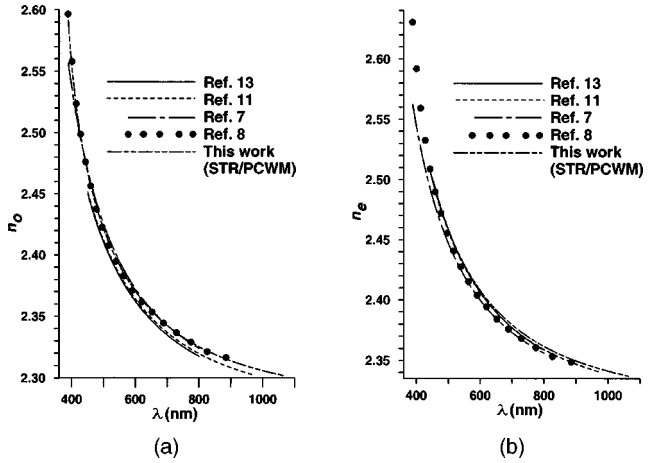

FIG. 5. (a) Comparative Sellmeier fits of the ordinary refractive index of GaN. The results of the correlated STR/PCWM results of sample No. 1 are compared with the Sellmeier fit to PCWM data for the MOCVD-grown sample (of Ref. 11), the Sellmeier fit of the PCWM data for the MBE-grown GaN sample (of Ref. 13), the Sellmeier fit of the SE data for the MOCVD-grown sample (of Ref. 7), and SE data for MBE-grown sample (of Ref. 8). All of these samples were grown on sapphire substrates except for the sample (described in Ref. 8) which was grown on SiC. The spectral ranges conform to the data used to generate the respective Sellmeier curves. (b) Comparative Sellmeier fit for the extraordinary index data, where the results of the present work were derived from PCWM only, with the same references.

deviate significantly in the vicinity of 400 nm. Turning our attention to comparisons of extraordinary index, the results of the PCWM analyses for n_e are consistent to within approximately 0.004. The deviation of the SE extraordinary index data of Yu *et al.*[7] with all of the PCWM results is generally larger, particularly in the range from 450–500 nm, as shown in Fig. 5(b). On the other hand, the SE results of Goldhaun *et al.*[8] for n_e agree to within approximately 0.006 for all of the PCWM results compared.

It is interesting to note that the overall agreement of the comparative refractive index results for GaN is fairly good and rather independent of the fabrication method. Deviations in the comparative SE results may be due to stray light arising from back surface reflections in spectral regions where the substrates are transparent. Such effects may explain the discrepancies between the SE results for n_o of Refs. 7 and 8 which utilized sapphire (absorption edge near 190 nm) and SiC (absorption edge near 500 nm), respectively. Furthermore, SE evaluation of n_e is further complicated by the fact that even at grazing incidence, the ray propagation angle in the GaN film is close to the normal (roughly 25° from the normal at 632 nm) making the contribution of the extraordinary index to the SE measurement difficult to extract. Thus, one would expect more consistent results for ordinary index measurements between SE studies, which is indeed the case observed.

As illustrated in Tables II(a) and II(b), values for sample thickness computed with TM modes are generally greater than the thickness results obtained with TE modes. The discrepancy in thickness between these two calculations is typically in the range of 10–20 nm, although for some of the samples, notably sample No. 6, the discrepancy is generally less than 10 nm. These discrepancies in L over all of the

samples are accommodated by our estimates in the uncertainty for the computed sample thickness, but the trend is nevertheless present. These effects are not necessarily associated with just the substrate/film buffer layers, even though they are comparable in magnitude to the buffer layer thickness used in MOCVD growth, as they are still observed in the HVPE-grown samples where buffer layers were not used. Returning to the GaN SE results reported by Yu *et al.*,[7] we also note that the thickness uncertainty they reported (42 nm) exceeds our estimate in thickness uncertainty by nearly a factor of 3. However, in the SE work of Goldhaun *et al.*,[8] the effects of a nonabrupt GaN/substrate interface are considered, and interlayers on both the GaN and SiC sides of the interface are included in their models. Such effects may arise from disorder, void formation, strain, and/or the filling of scratches in the substrate by GaN. The authors estimate that the thickness of these interlayers may extend tens of nms on either side of the interface. Additionally, contributions of interfacial anisotropy have also been attributed to anomalous effects observed in reflectance-difference spectroscopy studies of $Al_xGa_{1-x}N$ films.[23] Such effects may also help explain the observed optical scattering between TE and TM modes that we noted in some of the samples.

These observations lead us to speculate that the thickness discrepancies we observe could result from anisotropy in the defective interface region that exists between the films and sapphire substrates. This presumed anisotropy is then manifest by a slightly different optical thickness as measured by ordinary or extraordinary polarized light. It should be pointed out that a similar assumption about the refractive index in the film/substrate interface region was incorporated into the full model function used to fit to the STR data, which is discussed in detail elsewhere.[22] Specifically, the quantity (n_o-1) was assumed to be reduced from its ''bulk'' value (where bulk refers to the upper part of the film, not close to the interface) by as much as 7% in the film/substrate interface region, where the magnitude of the reduction factor for each film was determined as part of the curve-fitting procedure. In addition, examples of TEM images of the defective GaN/sapphire interface have been given by a number of authors.[24]

Finally, it is important to be aware that direct comparison of $Al_xGa_{1-x}N$ refractive indices between this research and earlier work is complicated by the large uncertainties, and possible systematic errors, in previous measurements of the Al mole fraction. For example, Bergman *et al.*[11] estimated a quantitative accuracy of $\pm 10\%$ for the Al mole fraction of the MOCVD-grown $Al_xGa_{1-x}N$ samples used in their work. Özgür *et al.*[13] calculated the Al mole fraction of their MBE-grown samples using bowing parameters derived from x-ray diffraction, optical absorption, and photoluminescence studies. However, they give no direct estimate of the uncertainty in the Al mole fraction in their samples but do remark on their observation that the bowing parameters should be dependent upon the growth method. The Al mole fraction results in the present work are believed to be more accurate (absolute uncertainty in x of ± 0.02) than those in previous work because our results are based on EDS measurements of each sample which were corrected for fluorescence and absorption effects and normalized to measurements of GaN and AlN reference samples. Any meaningful comparison of $Al_xGa_{1-x}N$ refractive index results (or other optical properties data) reported by different authors must take into account the measurement uncertainty of the Al mole fraction in each study as well as the measurement uncertainty of the refractive index (or other optical parameter). We have not attempted such a comparison in the present work.

X. SUMMARY

Using the methods of prism-coupling analysis and the birefringent waveguide theory, we have measured the wavelength-dependent refractive index and birefringence for a collection of $Al_xGa_{1-x}N$ samples grown by MOCVD and HVPE techniques. The Al mole fraction x, ranging from 0 to 0.666, was measured by EDS with an uncertainty of ± 0.02. The wavelength range spanned the interval from 442 nm to 1064 nm in several discrete steps, and the estimated uncertainty in the calculated refractive indices was ± 0.005. All of the waveguide refractive index data were fit by one-Sellmeier-term equations to within this uncertainty. In addition, we determined the ordinary refractive index within an extended wavelength range by curve-fitting analysis of spectroscopic, normal-incidence transmittance/reflectance (STR) measurements, correlated with the waveguide mode results. Two-Sellmeier-term equations were used for the curve-fitting analysis of the STR data. The short-wavelength limit of the range for the STR method varied from 363 nm for GaN, to 253 nm for $Al_{0.666}Ga_{0.334}N$; the long-wavelength limit was 2500 nm. The estimated uncertainty in the thickness of the samples was ± 15 nm, and the thickness results obtained from extraordinary-polarized modal data was generally 10–20 nm greater than the thickness obtained from the ordinary-polarized data. However, for some samples, the thickness discrepancy was substantially less. These discrepancies in the calculated values of film thickness could arise from anisotropy effects in the film/substrate interface region.

XI. DISCLAIMER

Reference to specific products or trade names does not constitute an endorsement by NIST. Other vendors may provide products of comparable or superior value.

[1] M. E. Lin, B. N. Sverdov, S. Strite, H. Morkoç, and A. E. Drakin, Electron. Lett. **29**, 1759 (1993).
[2] D. Brunner, H. Angerer, E. Bustarret, F. Freudenberg, R. Höpler, R. Dimitrov, O. Ambacher, and M. Stutzmann, J. Appl. Phys. **82**, 5090 (1997).
[3] G. Yu, H. Ishikawa, M. Umeno, T. Egawa, J. Watanabe, T. Soga, and T. Jimbo, Appl. Phys. Lett. **73**, 1472 (1998).
[4] G. Yu, H. Ishikawa, M. Umeno, T. Egawa, J. Wantanabe, T. Jimbo, and T. Soga, Appl. Phys. Lett. **72**, 2202 (1998).
[5] G. Yu, G. Wang, H. Ishikawa, M. Umeno, T. Soga, T. Egawa, J. Wantanabe, and T. Jimbo, Appl. Phys. Lett. **70**, 3209 (1997).
[6] U. Tisch, B. Meyler, O. Katz, E. Finkman, and J. Salzman, J. Appl. Phys. **89**, 2676 (2001).
[7] G. Yu, H. Ishikawa, T. Egawa, T. Soga, J. Watanabe, T. Jimbo, and M. Umeno, Jpn. J. Appl. Phys., Part 2 **36**, L1090 (1997).
[8] R. Goldhahn, S. Shokhovets, J. Scheiner, G. Gobsch, T. S. Cheng, C. T. Foxon, U. Kaiser, G. D. Kipshidze, and W. Richter, Phys. Status Solidi A **177**, 107 (2000).
[9] R. Ulrich and R. Torge, Appl. Opt. **12**, 2901 (1973).

[10] H. Y. Zhang, X. H. He, Y. H. Shih, M. Schurman, Z. C. Feng, and R. A. Stall, Appl. Phys. Lett. **69**, 2953 (1996).
[11] M. J. Bergman, Ü. Özgür, H. C. Casey, Jr., H. O. Everitt, and J. F. Muth, Appl. Phys. Lett. **75**, 67 (1999). See also M. J. Adams, *An Introduction to Optical Waveguides* (Wiley, New York, 1981). Note that Bergman's Eq. (3) that describes the TM modes appears to be incorrect. In order for the result to reduce to the expression, we derive (for the case of vanishing birefringence) and to be consistent with the form given by Adams, the factor ρ that distinguishes TM modes in Bergman's Eq. (3) should be set equal to 2 rather than equal to 1 as given.
[12] G. Webb-Wood, Ü. Özgür, H. O. Everitt, F. Yun, and H. Morkoç, Phys. Status Solidi A **188**, 793 (2001).
[13] Ü. Özgür, G. Webb-Wood, H. O. Everitt, F. Yun, and H. Morkoç, Appl. Phys. Lett. **79**, 4103 (2001).
[14] G. M. Laws, E. C. Larkins, I. Harrison, C. Molloy, and D. Somerford, J. Appl. Phys. **89**, 1108 (2001).
[15] S. Nikishin, G. Kipshidze, V. Kuryatkov, K. Choi, Ì. Gherasoiu, L. Grave de Peralta, A. Zubrilov, V. Tretyakov, K. Copeland, T. Prokofyeva, M. Holtz, R. Asomoza, Y. Kudryavtsev, and H. Temkin, J. Vac. Sci. Technol. B **19**, 1409 (2001).
[16] H. Angerer, D. Brunner, F. Freudenberg, O. Ambacher, M. Stutzmann, R. Höpler, T. Metzger, E. Born, G. Dollinger, A. Bergmaier, S. Karsch, and H.-J. Körner, Appl. Phys. Lett. **71**, 1504 (1997).
[17] B. N. Taylor and C. E. Kuyatt, *Guidelines for Evaluating and Expressing the Uncertainty of NIST Measurement Results*, NIST Technical Note, No. 1297, 1995 Edition (National Institute of Standards and Technology, Gaithersburg, MD, 1995).
[18] B. Lam, G. H. Gainer, S. Bidnyk, A. Elgawadi, G. H. Park, J. Krasinski, J. J. Song, D. V. Tsvetkov, and V. A. Dmitriev, Mater. Res. Soc. Symp. Proc. **639**, G6.4.1 (2001).
[19] A. Kazimirov, N. Faleev, H. Temkin, M. J. Bedzyk, V. Dmitriev, and Y. Melnik, J. Appl. Phys. **89**, 6092 (2001).
[20] J. Rams, A. Tejeda, and J. M. Cabrera, J. Appl. Phys. **82**, 994 (1997).
[21] *Devices Measurements and Properties*, Handbook of Optics Vol. II, edited by M. Bass (McGraw–Hill, New York, 1995,) p. 33.61.
[22] The complete model functions will not be described in detail here; a more complete account of the STR analysis will be presented in a forthcoming article: L. H. Robins, A. V. Davydov, A. J. Shapiro, N. A. Sanford, D. V. Tsvetkov, V. A. Dmitriev, S. Keller, U. K. Mishra, and S. P. DenBaars (unpublished).
[23] U. Rossow and D. E. Aspnes, Phys. Status Solidi A **177**, 57 (2000).
[24] Various authors have published cross-sectional TEM images illustrating highly defective layers near GaN/sapphire interfaces. See, for example, R. J. Molnar, in *Gallium Nitride (GaN) II*, Semiconductors and Semimetals Vol. 57, edited by J. I. Pankove and T. D. Moustakas (Academic, New York, 1999).